

## X-ray phase contrast for CO<sub>2</sub> microangiography

This article has been downloaded from IOPscience. Please scroll down to see the full text article.

2012 Phys. Med. Biol. 57 2603

(<http://iopscience.iop.org/0031-9155/57/9/2603>)

View [the table of contents for this issue](#), or go to the [journal homepage](#) for more

Download details:

IP Address: 130.237.32.230

The article was downloaded on 14/04/2012 at 20:15

Please note that [terms and conditions apply](#).

# X-ray phase contrast for CO<sub>2</sub> microangiography

U Lundström<sup>1</sup>, D H Larsson<sup>1</sup>, A Burvall<sup>1</sup>, P A C Takman<sup>1</sup>, L Scott<sup>2</sup>,  
H Brismar<sup>2</sup> and H M Hertz<sup>1</sup>

<sup>1</sup> Biomedical and X-Ray Physics, Department of Applied Physics, KTH Royal Institute of Technology/Albanova, 10691 Stockholm, Sweden

<sup>2</sup> Department of Women's & Children's Health, Karolinska Institute, S-17176 Stockholm, Sweden

E-mail: [ulf.lundstrom@biox.kth.se](mailto:ulf.lundstrom@biox.kth.se)

Received 11 September 2011, in final form 26 January 2012

Published 13 April 2012

Online at [stacks.iop.org/PMB/57/2603](http://stacks.iop.org/PMB/57/2603)

## Abstract

We demonstrate a laboratory method for imaging small blood vessels using x-ray propagation-based phase-contrast imaging and carbon dioxide (CO<sub>2</sub>) gas as a contrast agent. The limited radiation dose in combination with CO<sub>2</sub> being clinically acceptable makes the method promising for small-diameter vascular visualization. We investigate the possibilities and limitations of the method for small-animal angiography and compare it with conventional absorption-based x-ray angiography. Photon noise in absorption-contrast imaging prevents visualization of blood vessels narrower than 50 μm at the highest radiation doses compatible with living animals, whereas our simulations and experiments indicate the possibility of visualizing 20 μm vessels at radiation doses as low as 100 mGy. Experimental computed tomography of excised rat kidney shows blood vessels of diameters down to 60 μm with improved image quality compared to absorption-based methods. With our present prototype x-ray source, the acquisition time for a tomographic dataset is approximately 1 h, which is long compared to the 1–20 min common for absorption-contrast micro-CT systems. Further development of the liquid-metal-jet microfocus x-ray sources used here and high-resolution x-ray detectors shows promise to reduce exposure times and make this high-resolution method practical for imaging of living animals.

(Some figures may appear in colour only in the online journal)

## 1. Introduction

Visualization of blood vessels in small animals is of interest, e.g. in the study of angiogenesis. The growth of new blood vessels has a large impact on the development of cancer and other diseases (Folkman 2006). To assess the impact of new pharmaceuticals and treatments, and to clarify how tumors develop, noninvasive imaging methods capable of visualizing small blood

vessels in small animals are useful. There are several methods for this purpose, including x-ray micro-computed tomography ( $\mu$ CT), magnetic resonance imaging (MRI) and digital subtraction angiography (DSA) (Kagadis *et al* 2010, Badea *et al* 2008).  $\mu$ CT is based on x-ray absorption and provides a high-throughput, cost-effective method for three-dimensional (3D) imaging with relatively high resolution (Badea *et al* 2008). Using high doses of both contrast agent and radiation, this method has been shown to detect vessels with diameters down to 50  $\mu$ m (Kiessling *et al* 2004, Maehara 2003). Vessels smaller than this cannot be detected with acceptable radiation and contrast agent doses, due to fundamental photon noise from the quantization of x-rays.

In this paper, we demonstrate a  $\mu$ CT method based on phase-contrast x-ray imaging that allows the observation of smaller blood vessels at a lower dose than previously reported. Phase-contrast x-ray imaging relies on measuring the real (phase) part  $\delta$  of the refractive index  $n = 1 - \delta + i\beta$  instead of the imaginary (absorption) part  $\beta$  (Fitzgerald 2000, Wilkins *et al* 1996, Lewis 2004). The phase shift can be detected directly using interferometry (Momose *et al* 1996), via its derivative using crystal (Davis *et al* 1995) or grating systems (Momose 2005), or its second derivative using free-space propagation-based systems (Wilkins *et al* 1996).

Our 3D vascular imaging method relies on propagation-based phase-contrast imaging and injection of CO<sub>2</sub> gas as a contrast agent. The method is based on a laboratory source and has potential for the visualization of smaller blood vessels at a lower radiation dose than with the present small-animal imaging methods. A theoretical model, verified by 3D phantom experiments, shows that gas-filled vessels with diameters down to  $\sim 20$   $\mu$ m are detectable with a radiation dose of 100 mGy in small-animal-sized objects. CO<sub>2</sub>-contrast-based tomography of the vascular system in freshly excised rat kidneys shows vessels down to 60  $\mu$ m. Finally, a quantitative theoretical comparison between the state-of-the-art absorption  $\mu$ CT and our phase-contrast  $\mu$ CT provides the limits on the detectable vessel size as a function of dose for the two methods. Interestingly, the dose required to detect that a vessel scales with its size  $d$  approximately as  $d^{-2}$  for the propagation-based phase-contrast instead of  $d^{-4}$  as for the absorption contrast. Thus, the advantage of the phase-contrast method is for small vessels, while larger vessels are still better detected in absorption.

Previously, laboratory imaging of blood vessels using phase contrast and gas as a contrast medium has been presented by Laperle *et al* (2007, 2008). Using excised rat livers, the authors have developed a preparation method where the venous system is filled with air as the liver dehydrates. From the resulting difference in electron density between tissue and air, clear images of the venous system are obtained using a microfocus x-ray source. Apart from the careful consideration of the dose included in this paper, the main difference of the imaging methods lies in the application: the dehydration method is inherently for excised organs, while CO<sub>2</sub> injection is applicable to living animals. CO<sub>2</sub> gas is a clinically accepted contrast agent in absorption-based x-ray imaging (Cho and Hawkins 2007), but it has not previously been used with x-ray phase contrast. Other studies present phase-contrast imaging of blood vessels using synchrotron radiation. Momose *et al* (2000) use no contrast agent, but the high sensitivity of their interferometric method gives sufficient contrast. Lewis *et al* (2005) and Zhang *et al* (2008) image excised organs and Hwu *et al* (2004) living animals. In those three studies there is no mention of gas as a contrast medium, but considering the high contrast it seems likely that it is present through, e.g. accidental dehydration (Laperle *et al* 2008).

Other phase-contrast imaging of tissue involves, e.g., lungs, cartilage, breast and tumors (Lewis 2004, Momose 2005, Momose *et al* 2000, Hwu *et al* 2004, Hooper *et al* 2009) using synchrotron radiation at high doses, and mouse lungs (Lewis *et al* 2005) and guinea-pig joints (Coan and *et al* 2010) using microfocus sources at low doses but with lower resolution.

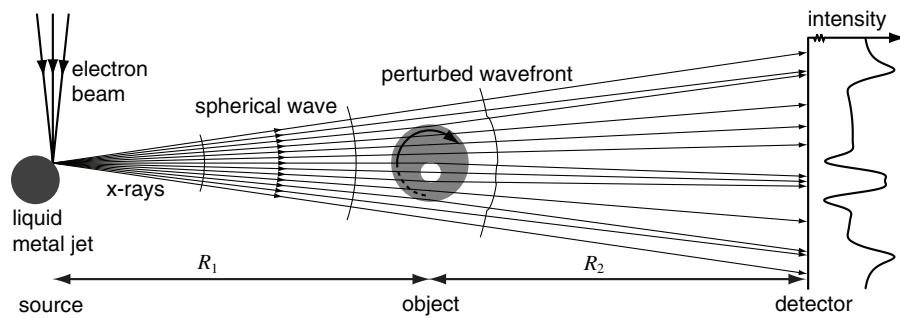


**Figure 1.** X-ray propagation-based phase-contrast imaging is used, a method that visualizes phase perturbations in the transmitted x-rays by letting them propagate a distance to the detector. As is illustrated in the center of the figure, a gas-filled blood vessel will focus the x-rays since the refractive index of the surrounding tissue is less than 1 at these wavelengths. We use a liquid-metal-jet microfocus x-ray source to achieve good coherence and decent exposure times. The object is rotated around a vertical axis for the tomographic imaging.

Additionally, phase-contrast imaging using gratings or microfocus sources has been performed on, e.g., fish, spiders, latex beads and dried organs (Wilkins *et al* 1996, Pfeiffer *et al* 2006, Tuohimaa *et al* 2007, Laperle *et al* 2007, 2008), typically allowing high doses to provide more detail.

## 2. Materials and methods

### 2.1. Imaging arrangement

Figure 1 illustrates the propagation-based (or in-line) x-ray phase-contrast method used for vascular imaging in this paper. It is based on cone-beam projection imaging with a source-to-object distance  $R_1 = 1.5$  m and object-to-detector distance  $R_2 = 1.5$  m, giving a magnification of  $M = (R_1 + R_2)/R_1 = 2$ . Phase contrast can be seen in these images if the system resolution is high enough (Mayo *et al* 2002). This can be understood from the refraction of x-rays at interfaces between materials of different density (e.g. tissue and gas). When the angle between the x-rays and the interface is small, as at the edge of a cylinder, the refraction angle can be detectable despite the small differences in the refractive index at these wavelengths (typically  $< 10^{-6}$ ). This gives rise to a bright fringe where the x-rays reach the detector, and a dark fringe where they otherwise would have, which effectively works as an edge enhancement to the normal absorption contrast also seen in the image. A more accurate way of understanding the imaging process, which we use for our simulations, is to consider the x-ray as an electromagnetic wave which is perturbed by the index of refraction variations in the object. By the free-space propagation of the wavefront to the detector, the phase shifts introduced by the object develop into intensity variations which can be measured. This method is not sensitive to the bandwidth of the x-ray spectrum, although there is an optimal energy with a good balance between x-ray penetration and contrast. By rotation of the object and acquisition of many images, a 3D dataset can be obtained through tomographic reconstruction.

The x-ray source is a liquid-metal-jet-anode microfocus source (Hemberg *et al* 2003), which operates at 50 kVp and 0.8 mA current with a  $7 \times 7 \mu\text{m}^2$  FWHM x-ray spot for the kidney images. For the plastic tube phantom, the electron beam current is instead 1.6 mA and the x-ray spot is  $12 \times 12 \mu\text{m}^2$ . The source is a modified prototype from Excillum AB

with Galinstan (GaInSn alloy) as a jet material. The detector is a scintillator-based fiber-coupled CCD detector from Photonic Science with  $9 \times 9 \mu\text{m}^2$  pixels over an area of  $36 \times 24 \text{ mm}^2$  and a  $5 \text{ mg cm}^{-2}$   $\text{Gd}_2\text{O}_2\text{S:Tb}$  scintillator. The CCD is read out with a bin level of 2 giving  $18 \times 18 \mu\text{m}^2$  pixels.

## 2.2. Phantom and kidney samples

Two objects were imaged. The first was a phantom intended for the verification of the accuracy of the theoretical model in section 4. It consists of four air-filled vertical low-density polyethylene (LDPE) tubes with inner diameters ranging from 23 to  $684 \mu\text{m}$  placed in a water-filled cylindrical PMMA holder of 16 mm inner diameter and 22 mm outer diameter. In absorption, this corresponds to about 21 mm of tissue, a typical object thickness in small-animal imaging. LDPE was chosen because of its density, which is similar to that of water and tissue, thus making the tubes a proper blood vessel phantom.

The second object was a rat kidney injected with  $\text{CO}_2$  gas to show that the method works on biological samples. The kidney was placed in a physiological solution in a cone-shaped holder with 1 mm thick PMMA walls. The venous system was filled with  $\text{CO}_2$  through a tube inserted in the renal vein.  $\text{CO}_2$  is a clinically accepted contrast medium in absorption x-ray imaging (Cho and Hawkins 2007). The gas pressure was monitored and kept at  $40 \pm 10$  mbar. The kidneys were retrieved from rats following the regulations of the Institutional Animal Care and Use Committee of Karolinska Institute and imaged within a few hours of excision.

## 2.3. Image reconstruction

A 3D representation of the object is obtained through tomographic reconstruction using filtered back projection in cone-beam geometry with the Octopus software package (Vlassenbroeck *et al* 2007). The object is rotated around its vertical center axis, with images recorded at steps of one or half a degree.

For the reconstructed volume data to represent density, so that it can be automatically segmented, the input for the tomographic-reconstruction algorithm must be the projected density. There exist several phase-retrieval algorithms for converting phase-contrast images into the projected density (Burvall *et al* 2011). We have chosen a Fourier-based algorithm developed by Paganin *et al* (2002), which assumes the object to consist of only one material, or more generally that the local absorption coefficient is proportional to the phase-shifting parameter  $\delta$ . This is a good assumption when the object consists of only tissue and gas with negligible absorption and phase shift, but would smooth out interfaces between, e.g., bone and tissue. Parameters for absorption coefficient and phase shifts are taken from NIST (Hubbell and Seltzer 2011) and RTAB (Kissel 2000) for an energy of 20 keV, at the center of the used x-ray spectrum.

## 2.4. Numerical modeling

The phase-contrast imaging system is simulated through the numerical evaluation of the Fresnel diffraction integral (Goodman 2004). The x-ray intensity  $I$  at the detector is calculated using fast Fourier transform as

$$I(x, y, z) \propto \left( F^{-1} \left\{ F\{g(x, y)\} \cdot \exp\left(- (u^2 + v^2) \frac{2\pi^2 z}{ik}\right) \right\} \right)^2. \quad (1)$$

Here  $F$  denotes the Fourier transform,  $x$  and  $y$  are the transverse coordinates,  $g(x, y) = \exp(i\varphi(x, y) + \tilde{\mu}(x, y)/2)$  is the transmission function of the object, where the linear absorption

$\tilde{\mu}(x, y) = \int \mu(x, y, z) dz$  and phase shift  $\varphi(x, y) = \int k\delta(x, y, z) dz$  are calculated with the absorption coefficient  $\mu = \beta \cdot 4\pi/\lambda$  from NIST (Hubbell and Seltzer 2011) and  $\delta$  from RTAB (Kissel 2000). The exponential term in equation (1) is the free-space propagator, where  $u$  and  $v$  are spatial frequencies and  $k$  is the wavenumber. The propagation distance  $z = \frac{R_1 R_2}{R_1 + R_2}$  of this classical plane-wave model is the object-to-detector distance modified by the magnification to take the spherical wave geometry from the source into account (Paganin *et al* 2002). The resulting image intensity  $I(x, y)$  is then convolved with the measured point-spread function of the detector (FWHM  $\approx 22 \mu\text{m}$ ) and the measured source intensity distribution scaled to the detector plane. Individual calculations are performed for the different energies of the source spectrum (typically ten energy bins) and added to produce the spectrally integrated image. Photon noise is simulated as a random Poissonian probability distribution for each energy bin, given the quantitative photon numbers of the source spectrum. The spectrum is compensated for incomplete absorption in the detector and absorption in air and other materials between the source and detector. In this way, the expected detector signal and variance in each pixel can be calculated, and by modifying the noise power spectrum (NPS) to that of the detector, an image very similar to what one would get in reality is obtained. As x-ray photon noise and electronic readout noise are the two main sources of noise, only these two are taken into account in the simulations.

### 2.5. Dose control

The radiation dose is kept low to show that this imaging modality gives good image quality at low doses. It is calculated as the average dose over the object from a measured x-ray spectrum using mass energy-absorption coefficients from NIST (Hubbell and Seltzer 2011). The dose calculations were verified by measurement with an ionization chamber.

## 3. Experimental results

Figure 2 shows imaging of the air-filled LDPE-tube phantom, comparing the experiment (figures 2(a), (c) and (e)) with numerical simulation (figures 2(b), (d) and (f)). The 16 mGy projection images show good agreement between the experiment (figure 2(a)) and numerical simulation (figure 2(b)). They are averaged in the vertical direction to give the profile plots below (figures 2(c) and (d)). Figures 2(e) and (f) show tomographic slices of the phantom, perpendicular to the tubes and the rotational axis, reconstructed from experimental and simulated data, respectively. The source was running at the 1.6 mA electron beam current with a  $12 \times 12 \mu\text{m}^2$  x-ray spot. The 180 projections over  $180^\circ$  had an exposure time of 20 s each, giving a total exposure time of 60 min and a total radiation dose of 160 mGy. The presented slices are 3 voxels thick ( $27 \mu\text{m}$ ), to present the information of a length of the vessels approximately equal to the diameter of the smallest tube. All tubes are visible even in a  $9 \mu\text{m}$  thick slice. Even the  $23 \mu\text{m}$  tube is clearly visible, something that would require at least 100 times higher dose with conventional iodinated contrast agents. This is further discussed in section 4 where a comparison between phase and absorption contrast is given. Experiments and simulations are in good agreement with respect to contrast, noise level and general appearance.

Figure 3 shows phase-contrast imaging of the CO<sub>2</sub>-filled venous system of a rat kidney. Figure 3(a) is a single projection image clearly showing blood vessels down to  $60 \mu\text{m}$  in diameter, despite the low dose of 10 mGy. The large number of overlapping vessels makes many of them difficult to separate. For this reason, the tomographic reconstruction (figures 3(b)–(d)) is preferable. It is made from 360 phase-retrieved projections with 14 s

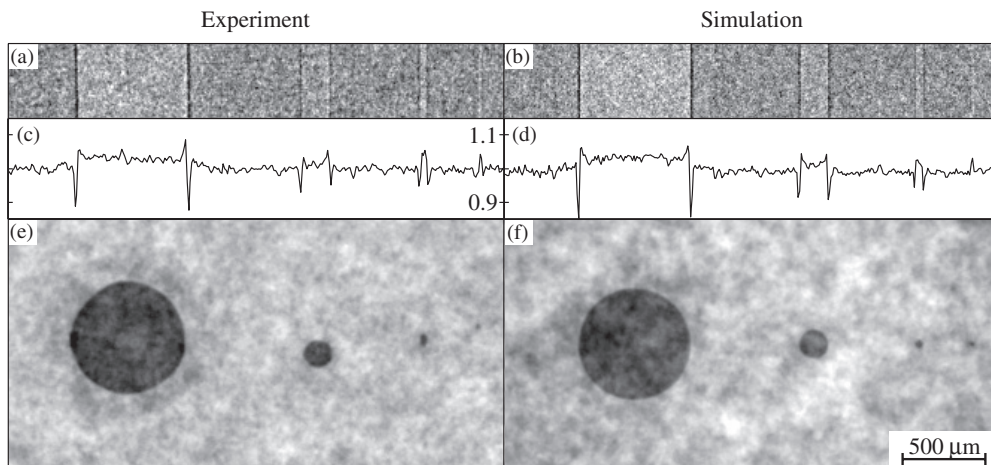


**Figure 2.** Experimental (a) and simulated (b) images of a phantom consisting of four gas-filled plastic tubes of inner diameters 684, 176, 50 and 23  $\mu\text{m}$  immersed in water. The gray scale is linear from 0.85 (black) to 1.15 (white) of the average background value. The exposure time is 6 min, corresponding to 16 mGy of radiation dose. (c) and (d) show the images above them averaged vertically. (e) and (f) show two 27  $\mu\text{m}$  thick slices in tomographic reconstruction of the phantom made from experimental (e) and simulated (f) data. The reconstructions are made from 180 phase-retrieved projections over  $180^\circ$  with a total exposure time of 1 h and a radiation dose of 160 mGy. The 500  $\mu\text{m}$  scale bar applies to all image parts.

exposure time each over  $180^\circ$ , giving a total radiation dose of 160 mGy. It is here presented with a horizontal slice (figure 3(c)) and as 3D renderings of an isosurface from above (figure 3(d)) and in the direction of the first projection (figure 3(b)). The relatively high contrast compared to the noise level as seen in the slice makes it easy to automatically separate vessels from tissue for visualization or computer analysis. The dark corners of figure 3(c) are due to air outside the conically shaped PMMA holder. In figure 3(d), the lack of vessels in the center of the kidney can be seen. The plastic tube in the upper-left corner of figures 3(a) and (b) was used to inject  $\text{CO}_2$ .

#### 4. Theoretical and numerical modeling

To assess whether the phase contrast and  $\text{CO}_2$  can be useful in microangiography, we compare the capability of detecting blood vessels in a mouse using the present method to  $\mu\text{CT}$  using contrast agents based on iodine. As a measure of image quality, and to determine whether a blood vessel can be detected, we use statistical decision theory. More specifically, we calculate the signal-to-noise ratio (SNR) in the test statistic of the ideal observer for detection in a signal-known-exactly/background-known-exactly task (Barrett and Myers 2004). This gives an objective measure of the amount of reliable information that is present in an image. A more sophisticated observer model such as the channelized Hotelling observer would better resemble a human viewing the images. This would however move the focus from the imaging task to post-processing, reconstruction and the observer.

The test statistic of the ideal observer is accurately modeled as Gaussian, since it is a weighted sum of many pixel values, with contributions from a total of many photons. Since the contrast is low, the variance in the test statistic is approximately equal in the cases of

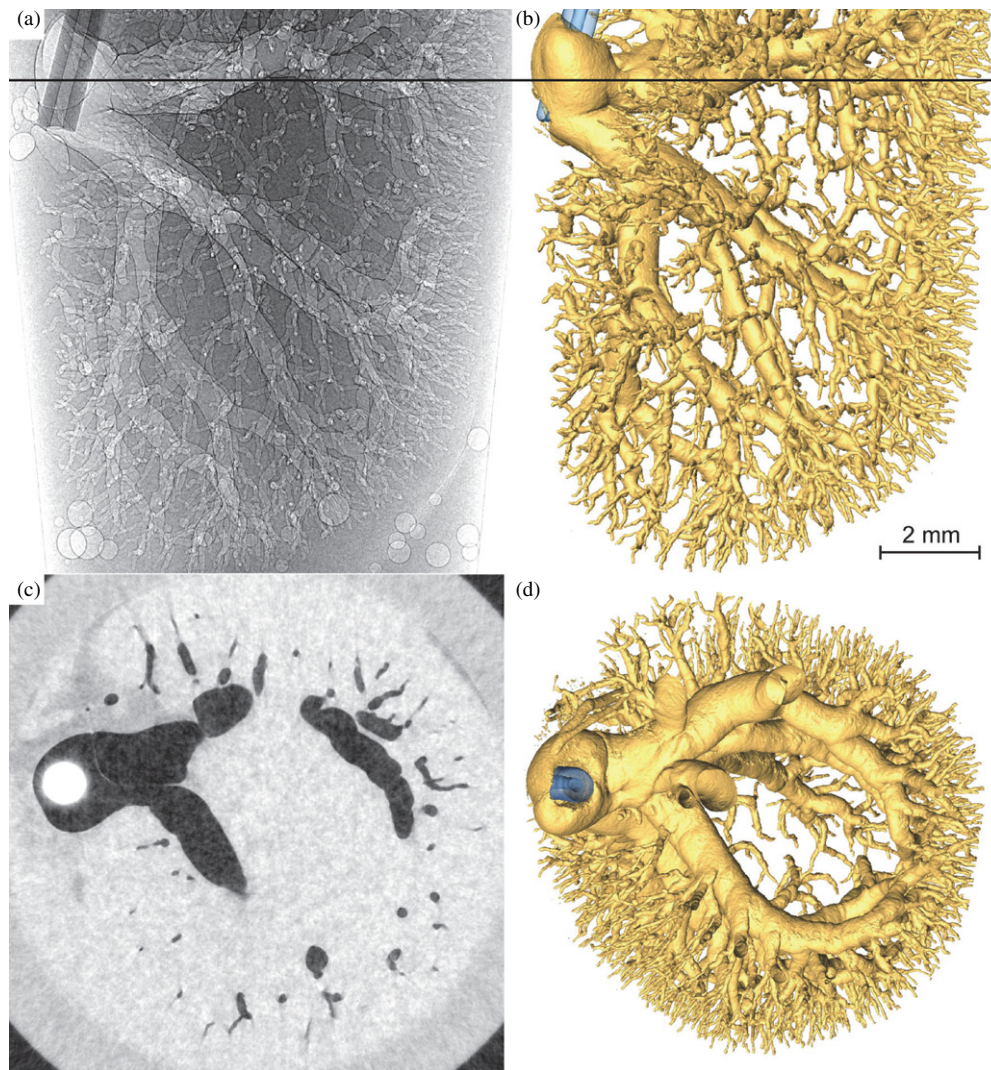


**Figure 3.** X-ray propagation-based phase-contrast images of a rat kidney with its venous system injected with CO<sub>2</sub> gas. (a) An unprocessed 10 mGy (5 min) single projection. The tomographic reconstruction from 360 14 s projections over 180° with a total radiation dose of 160 mGy is shown as an isosurface (b) and (d) and with a horizontal slice (c) corresponding to the line through (a) and (b). The vessels have been gas filled down to diameters of 60–100 μm and all gas-filled vessels are clearly visible and automatically segmentable. The 2 mm scale bar applies to all image parts.

signal-present and signal-absent. With these approximations in the imaging model, the ideal observer statistic is linear in data, and therefore equivalent to the Hotelling observer (Barrett and Myers 2004).

The ideal observer SNR<sup>2</sup> needed for an object to be detectable by the human eye is about 25 (Rose 1948). Blood vessels will get different SNRs depending on their lengths. To avoid this problem, we will always calculate the SNR<sup>2</sup> for a length of the vessel equal to its width, and set the visibility threshold to SNR<sup>2</sup> = 25. Pieces of a vessel shorter than its width will thus not be detectable, while longer parts will. This indicates the possibility of tracking a vessel.

The mouse is modeled as a 20 mm thick piece of soft tissue (with elemental composition as tabulated by NIST (Hubbell and Seltzer 2011)). The blood vessels are modeled as cylinders with diameters from 10 to 1000  $\mu\text{m}$ , approximately the range found in mice that have any hope of being visualized. These cylinders are in the phase-contrast case filled with  $\text{CO}_2$  gas, and in the absorption case filled with contrast agents with appropriate absorption coefficients. We assume the tissue to be homogeneous, since the inhomogeneities that exist result in very low modulation compared to the photon noise. The variations in absorption and refractive index within the tissue are also negligible compared to the difference with the contrast agents, making structural noise unimportant in the tomographic reconstruction.

#### 4.1. Absorption contrast model

To avoid comparison with a specific  $\mu\text{CT}$  system, we consider a perfect imaging system in the absorption-contrast case. Hence, the system has infinite resolution, no noise other than intrinsic x-ray photon noise detects every unscattered photon reaching the detector, and uses monochromatic 35 keV x-ray radiation. Because of the relatively low resolution required in absorption-contrast imaging, detectors can be made quite efficient, and thus the assumption of perfect detection is often not that farfetched. When imaging vessels smaller than 50  $\mu\text{m}$ , non-ideal detector performance will definitely be a problem, but at these sizes the conclusion drawn below is still that phase contrast outperforms any absorption contrast system. The other difference compared to a real system with considerable impact on image quality is the x-ray spectrum. A monochromatic spectrum just above the iodine absorption edge at 33.2 keV can be achieved at a synchrotron, but not with an x-ray tube. The capabilities we present for absorption contrast systems will thus be an upper bound on what any real system could achieve.

Because of these idealizations, the system is readily handled theoretically. Starting from equation (13.119) in Barrett and Myers (2004), one can derive (see the [appendix](#)) the following expression for the dose  $D$  required to obtain a certain  $\text{SNR}^2$  for a cylinder of length and diameter  $d$ :

$$D = \frac{3E (1 - e^{-\mu_{\text{en}}t_0}) e^{\mu_0 t_0} \text{SNR}^2}{2t_0 \rho d^4 (\mu_1 - \mu_0)^2}. \quad (2)$$

In this equation,  $E = 35$  keV is the photon energy,  $t_0 = 20$  mm and  $\rho = 1060$   $\text{kg m}^{-3}$  are the thickness and density of the tissue surrounding the cylinder,  $\mu_{\text{en}} = 10.4$   $\text{m}^{-1}$  and  $\mu_0 = 32.1$   $\text{m}^{-1}$  are the energy-absorption coefficient and attenuation coefficient of the tissue (NIST soft tissue) and  $\mu_1$  is the attenuation coefficient of the blood and contrast agent mixture. The CT numbers 500, 1000 and 2000 Hounsfield units (HU) used in figure 5 corresponds to  $\mu_1 = 46.2$ , 61.6 and 92.4  $\text{m}^{-1}$ , respectively, at 35 keV.

The limit on injected concentrations of contrast agents is ultimately decided by their toxicity. We have compared six papers (Kiessling *et al* 2004, Badea *et al* 2005, 2006, Mukundan *et al* 2006, Rabin *et al* 2006, Schambach *et al* 2010) using absorption contrast agents and  $\mu\text{CT}$  for small-animal angiography. Table 1 summarizes the contrast agent concentrations used and the obtained CT numbers. The concentrations of contrast agents in the blood are calculated from the injected amounts and the assumption of 80 ml of blood per kg animal. These values fall in the range of 8–26  $\text{mg ml}^{-1}$  blood, which at 35 keV corresponds to CT numbers of 600–2700 HU. The actual CT numbers are lower because of the broad x-ray spectrum. They are in the range from 520 to 900 HU, except possibly for the paper by Kiessling *et al* (2004), in which the CT number is not stated but could be as high as 2000 HU. The table also contains the radiation doses used and the sizes of the smallest detectable blood vessels as stated in the papers. Finally, we note that the exposure times typically are in the range from 1 to 20 min.

**Table 1.** Information extracted from publications on small-animal x-ray angiography. The I or Bi concentration in the blood is calculated from the reported injected volumes of contrast agents assuming the animals to have 80 ml of blood per kg of body weight. The radiation dose used and the size of the smallest detectable vessels are shown for comparison.

Paper	Contrast agent	I/Bi concentration in blood (mg ml <sup>-1</sup> blood)	Maximum CT number (HU)	Radiation dose (mGy)	Detectable vessel diameter (μm)
Mukundan <i>et al</i>	Iodine-filled liposomes	26	900	–	~1000
Kiessling <i>et al</i>	Iomeprol	–	–	140	~50
Badea <i>et al</i> 2005	Fenestra VC	12	620	920	–
Badea <i>et al</i> 2006	Fenestra VC	12	518	220	~100
Schambach <i>et al</i>	Fenestra VC	20	–	2000	~50
Rabin <i>et al</i>	Bismuth sulfide	8	550	–	–

#### 4.2. The phase-contrast model

The image quality is evaluated based on the simulations of section 2.4 with the same system parameters and geometrical arrangement as for the phantom imaging described in section 2.2. For this system, the NPS of the detector has a large impact on the resolution, which in turn affects the contrast. To handle this, we assume the system to be continuous, shift-invariant and to have Gaussian noise, so that we can calculate the SNR in the Fourier plane from equation (13.236) in Barrett and Myers (2004):

$$\text{SNR}^2 = \iint \frac{|\Delta G(\mathbf{u})|^2}{W(\mathbf{u})} d^2u, \quad (3)$$

where  $\mathbf{u}$  is the spatial frequency,  $\Delta G$  is the Fourier transform of the difference in expected images, with and without an object and  $W$  is the NPS. The expected image with an object is calculated as is explained in section 2, with all imaging parameters set as for the phantom imaging. Without an object, the expected image is simply the constant expected background value. The NPS has one constant contribution from readout noise and one exposure-dependent contribution from photon noise, weighted down for higher frequencies as the resolution of the detector drops off. The integral in equation (3) is evaluated numerically and the exposure required to give  $\text{SNR}^2 = 25$  is found through iteration. The radiation dose corresponding to the obtained exposure is calculated as explained in section 2.

#### 4.3. Extension to tomography

The derivations of equations (2) and (3) are made for 2D images, but as shown in Hanson (1979), the ideal observer  $\text{SNR}^2$  of a tomographic reconstruction will be the same as the total  $\text{SNR}^2$  in the projections. For a rotationally symmetric object (e.g. a cylinder), all projections are the same. If readout noise can be neglected, the ideal observer  $\text{SNR}^2$  is proportional to the exposure time. The  $\text{SNR}^2$  will, thus, be the same for a tomogram, as for a single projection with the same total exposure time. Equation (2), which is derived for a perfect projection image, is thus equally valid for a tomographic reconstruction as for a single image.

Including readout noise, as is needed when using equation (3) for tomography, the  $\text{SNR}^2$  will decrease with increasing number of projections. For our simulations, we use 180 projections as in the phantom experiments. This is enough to make the artifacts caused by the low number of projection angles negligible compared to statistical noise. In this case, each projection should have an  $\text{SNR}^2 = 25/180$ , and the total exposure is 180 times that of each projection.

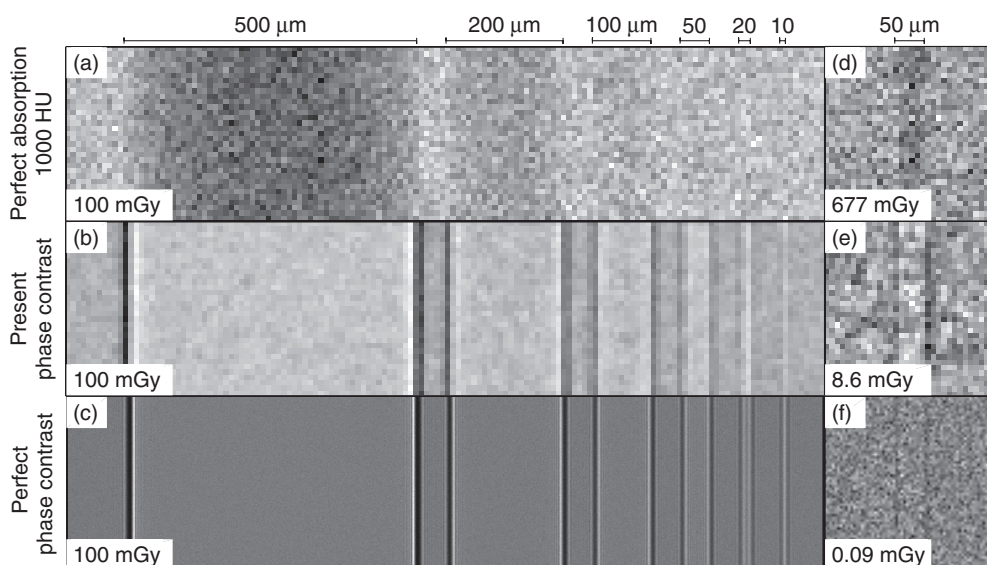


**Figure 4.** Simulated images comparing phase contrast using  $\text{CO}_2$  and absorption contrast using iodine. (a)–(c) show 100 mGy images of cylinders with diameters 500, 200, 100, 50, 20 and  $10 \mu\text{m}$  in 2 cm thick tissue. The images are for a perfect absorption system and 1000 HU absorption (a), our present phase-contrast system (b) and a perfect phase-contrast system (c). With 1000 HU absorption, a dose of 100 mGy is almost enough to observe a  $100 \mu\text{m}$  diameter vessel. Using phase contrast and  $\text{CO}_2$ ,  $20 \mu\text{m}$  vessels are visible and even  $10 \mu\text{m}$  vessels can be detected if they are long enough. (d)–(f) illustrate the ideal observer SNR measure by showing the images of a  $50 \mu\text{m}$  diameter cylinder at doses adjusted to give  $\text{SNR}^2 = 25$  for a length equal to the diameter of the vessel. The grayscales are linear with ranges in normalized intensity of 0.98–1.02 (a), 0.75–1.13 (b), 0–2.7 (c), 0.995–1.005 (d), 0.82–1.15 (e) and 0–3.5 (f).

The phase retrieval does not change the  $\text{SNR}^2$  of an image, since it is reversible and thereby cannot remove any information from the image. This can also be understood from the fact that the phase retrieval algorithm for low contrast images only does a reweighting of different spatial frequencies, which is ignored by equation (3).

#### 4.4. Results

Figures 4 and 5 compare our phase-contrast method with absorption contrast. Figures 4(a)–(c) give a visual comparison showing how 2D imaging of a model system with different diameter vessels will look in absorption and phase contrast at the 100 mGy radiation dose. The absorption system is simulated as perfect, as described above, except for the finite ( $9 \mu\text{m}$ ) pixel size required for visualization. With 1000 HU absorption, the 500 and  $200 \mu\text{m}$  vessels are clearly visible, while the  $100 \mu\text{m}$  vessel is just detectable. With our present phase-contrast system, vessels down to  $20 \mu\text{m}$  are clearly visible, while the  $10 \mu\text{m}$  vessel can only be observed because of its unrealistic straightness. For a theoretical perfect phase-contrast system, 100 mGy is more than enough to clearly visualize any  $\text{CO}_2$ -filled vessels.

Figures 4(d)–(f) show the appearance of  $50 \mu\text{m}$  vessels with the radiation doses adjusted so that our model observer considers them to be on the detection limit, i.e.  $\text{SNR}^2 = 25$  for a length equal to the width of the vessel. The vessels are quite easily observed in these images, since the length shown is larger than the width, and thus the total  $\text{SNR}^2$  is 125 instead of 25.

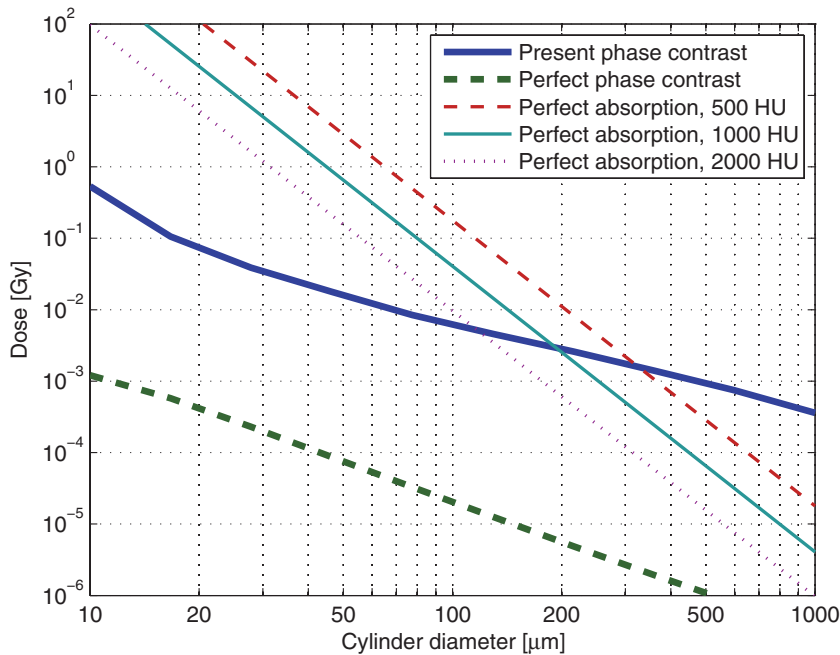


**Figure 5.** Comparison between propagation-based phase-contrast imaging using CO<sub>2</sub> as a contrast agent and conventional absorption-contrast imaging using iodinated contrast agents for tomography. The graphs show the radiation dose required to detect a blood vessel in 20 mm thick tissue as a function of its diameter. The phase-contrast system is simulated with a source-to-object distance of 1.5 m and a source-to-detector distance of 3 m. For the ‘present phase-contrast’ line source and detector limitations such as limited detector absorption efficiency, resolution, readout noise and a broad x-ray spectrum are taken into account, while for the ‘perfect phase contrast’ and absorption lines these are neglected to show the fundamental physical limits of the two methods. The absorption lines are obtained from equation (2) and agree exactly with what can be obtained from the simulation tool used for the phase-contrast lines.

Note the two-four orders of magnitude difference in the required dose between the phase and absorption methods. Finally, we note that in figure 4(d) the dose is slightly lower than indicated in figure 5, since the readout noise causes a difference between a single projection and tomography.

Figure 5 gives a more quantitative comparison for tomography using the model observer. The radiation dose required to detect a vessel is plotted as a function of the vessel diameter for phase-contrast imaging using CO<sub>2</sub> and absorption-contrast imaging. In the absorption case, the dose will depend on the contrast agent concentration in the blood and is therefore plotted for three different CT numbers, 500, 1000 and 2000 HU, where the middle one is probably the most relevant. These lines are calculated using equation (2), but the exact same lines are obtained when using the same numerical method as for phase-contrast imaging. In the phase-contrast case, the required dose is plotted both for our present imaging arrangement and for a perfect arrangement with the same imaging distances, but with a monochromatic point source and a perfect detector. The graph is based on the same simulations as those used for figure 4.

The absorption contrast systems in figure 4 follow the  $d^{-4}$  dependence of equation (2). Consequently, absorption imaging requires a very high dose for detecting the smallest vessels. The ‘perfect phase-contrast’ system, on the other hand, can be seen to essentially exhibit a

$d^{-2}$  dependence on vessel diameter. For larger vessels ( $>1$  mm), it will converge toward the 1000 HU absorption contrast line since absorption contrast in the images will start to dominate. Our ‘present phase-contrast’ system has a steeper than  $d^{-2}$  dependence for the smallest vessels due to the limited resolution of the system, while for the larger vessels it is flatter than  $d^{-2}$  since readout noise prevents the dose from decreasing more rapidly.

## 5. Discussion

It is clear that the propagation-based phase contrast provides improved imaging of small vessels, since the dose required to detect a vessel scales as  $d^{-2}$  for phase contrast versus  $d^{-4}$  for absorption contrast. From figure 4, we note that phase-contrast imaging has the potential to either reduce the radiation dose several orders of magnitude with the maintained image quality or to lower the detection limit an order of magnitude with constant dose. Already our present system is capable of detecting smaller vessels than what is theoretically possible using an absorption-contrast system with limited dose. With a radiation dose of 100 mGy, an absorption system with 1000 HU of contrast cannot detect any vessels below  $80\ \mu\text{m}$ , while the limit for our system is  $<20\ \mu\text{m}$ . The present phase-contrast system is better than absorption with respect to dose for vessels smaller than roughly  $200\ \mu\text{m}$ .

To obtain good contrast in propagation-based phase-contrast imaging, high resolution is required, i.e. small source spot size and high detector resolution. A small spot size implies low power and thereby long exposure times. For the detectors, high resolution can only be achieved with low detection efficiency, which gives unnecessarily high dose and exposure time. Fortunately, new sources (Hemberg *et al* 2003) and detector concepts (Svenonius *et al* 2009) are being developed, which show promise for improved exposure time, detection efficiency and resolution. Figure 4 shows that the dose required to detect a  $100\ \mu\text{m}$  diameter vessel at  $\text{SNR}^2 = 25$  can theoretically be reduced  $300\times$  compared to the present system. The primary factors limiting image quality are the low absorption efficiency of the detector and the limited resolution of the system (i.e. detector resolution and source spot size). If the imperfections are removed one after the other in the following order, they give reductions in dose with these factors: readout noise  $1.8\times$ , detector absorption efficiency  $6.3\times$ , resolution  $8.4\times$  and spectrum  $3.0\times$ . The new sources and detectors currently under development are not easily going to give us this factor of 300, but there is room for significant improvement.

From the discussion above, it is clear that the phase-contrast imaging process would allow the detection of  $<20\ \mu\text{m}$  vessels provided that the density difference can be obtained. In figure 3, we observe vessel sizes only down to  $60\ \mu\text{m}$ . However, the minimum size is not limited by the imaging process but by insufficient penetration of  $\text{CO}_2$  into the vascular system. The  $\text{CO}_2$  gas has lower viscosity than blood which makes it flow easier through the vessels but the surface tension of the gas–liquid interface hinders it from entering the smallest vessels. An upper bound on how far into the vascular system it will reach can be calculated from the equilibrium between gas pressure and surface tension (although it is difficult to predict how quickly the  $\text{CO}_2$  will dissolve). The relevant forces on the gas–liquid surfaces are from gas pressure,  $F_p = \frac{\pi}{4}D^2P$ , and from surface tension,  $F_\gamma = \pi D\gamma \cos\theta$  (de Gennes *et al* 2004). Here,  $D$  is the vessel diameter at the meniscus,  $P$  is the pressure difference over the surface,  $\gamma$  is the surface tension of the blood and  $\theta$  is the contact angle. In our phase-contrast images, we can see that  $\theta$  is either very close to or equal to 0. Assuming  $\theta = 0$  and equating the forces gives us

$$D = \frac{4\gamma}{P}. \quad (4)$$

Assuming the surface tension of blood to be  $\gamma = 52 \text{ mN m}^{-1}$  (Rosina *et al* 2007) and the pressure difference to be  $P = 100 \text{ mbar}$ <sup>3</sup>, we obtain a diameter  $D \approx 20 \text{ }\mu\text{m}$ . Thus, it appears that also the penetration of the CO<sub>2</sub> contrast medium should allow detection down to  $20 \text{ }\mu\text{m}$  vessels at physiologically relevant conditions. The images presented in this paper have been taken with pressures of about  $40 \text{ mbar}$ , which would give  $D \approx 50 \text{ }\mu\text{m}$ , not far from the  $60 \text{ }\mu\text{m}$  seen in the images.

The implementation of x-ray imaging with  $\sim 10 \text{ }\mu\text{m}$  resolution in live samples will induce problems due to motion blurring from respiratory and cardiac motion. One solution is short exposure times. Unfortunately, no microfocus tubes with higher power than the liquid-jet system used here exist. On a longer term, however, the liquid-jet x-ray source can potentially be scaled to higher powers because of the regenerative nature of the anode (Hemberg *et al* 2004). Lung and heart gating can reduce motion blur to less than  $100 \text{ }\mu\text{m}$  (Mai *et al* 2005), but to obtain lower than  $10 \text{ }\mu\text{m}$  will be a challenge. Another technique is to use mechanical breathing and stop it for a short time while taking an image. This technique combined with improved sources and detectors should make it possible to image whole small animals with high resolution, except the region closest to the heart.

Finally, we note that the phase-contrast system inherently needs more space than a comparable absorption-contrast system. The contrast is essentially proportional to the propagation distance, which makes the required radiation dose proportional to the inverse square of the length of the system. We have chosen a source-to-detector distance of  $3 \text{ m}$  as this is a reasonable system length and still gives a great advantage over absorption contrast. A longer distance will give lower dose, but somewhat longer exposure times.

## Acknowledgments

This work was supported by the Swedish Science Research Council, the Swedish Foundation for Strategic Research and the Wallenberg Foundation.

## Appendix. Absorption contrast dose

The radiation dose  $D$  required to detect a cylinder imaged sideways using x-ray absorption contrast can be calculated theoretically. We assume that the cylinder has a length and diameter  $d$ , absorption coefficient  $\mu_1$ , is placed in  $t_0$  thick soft tissue with the attenuation coefficient  $\mu_0$ , energy-absorption coefficient  $\mu_{\text{en}}$  and density  $\rho$  and imaged with a perfect detector and monochromatic x-rays of photon energy  $E$ . With an incoming fluence (photons per area)  $\Phi_0$  and the assumption of low contrast, the fluence at the detector placed just behind the object will be

$$\Phi = \Phi_0 e^{-\mu_0 t_0 - (\mu_1 - \mu_0)t(x)} \approx \Phi_1 (1 - (\mu_1 - \mu_0)t(x)),$$

where

$$\Phi_1 = \Phi_0 e^{-\mu_0 t_0}$$

and

$$t = \begin{cases} 2\sqrt{d^2/4 - x^2} & |x| < d/2 \\ 0 & |x| \geq d/2 \end{cases}$$

<sup>3</sup> The pressure drop over the small arteries and arterioles is about  $65 \text{ mm Hg}$  in humans with mean arterial pressure (MAP)  $95 \text{ mm Hg}$  (Boron and Boulpaep, 2009). If mice with  $112 \text{ mm Hg}$  (Mattson, 2001) has the same fraction of the pressure drop over the small arteries and arterioles it would be  $77 \text{ mm Hg} = 100 \text{ mbar}$ .

If each pixel has a small area  $A$ , the number of photons reaching a pixel will be  $N = A\Phi$  and the SNR can be calculated by summing overall pixels (Barrett and Myers 2004, equation (13.119)):

$$\begin{aligned} \text{SNR}^2 &= \sum \frac{(N - N_1)^2}{\sigma^2} = \sum \frac{[A(\Phi - \Phi_1)]^2}{A\Phi_1} = \Phi_1 \sum A[(\mu_1 - \mu_0)t]^2 \\ &= \Phi_1 \int_{-d/2}^{d/2} dx \int_0^d dy [(\mu_1 - \mu_0)t]^2 \\ &= \Phi_1 (\mu_1 - \mu_0)^2 d \int_{-d/2}^{d/2} 4 \left( \frac{d^2}{4} - x^2 \right) dx = \Phi_0 e^{-\mu_0 t_0} (\mu_1 - \mu_0)^2 \frac{2}{3} d^4. \end{aligned}$$

By demanding a certain  $\text{SNR}^2$  (e.g. 25), we can calculate the required incoming fluence

$$\Phi_0 = \frac{3}{2} \frac{\text{SNR}^2 e^{\mu_0 t_0}}{(\mu_1 - \mu_0)^2 d^4}.$$

This will give a radiation dose of

$$D = \frac{E\Phi_0 (1 - e^{-\mu_{en} t_0})}{t_0 \rho} = \frac{3E (1 - e^{-\mu_{en} t_0}) e^{\mu_0 t_0} \text{SNR}^2}{2t_0 \rho d^4 (\mu_1 - \mu_0)^2}.$$

## References

- Badea C T, Drangova M, Holdsworth D W and Johnson G A 2008 *In vivo* small-animal imaging using micro-CT and digital subtraction angiography *Phys. Med. Biol.* **53** R319–50
- Badea C T, Fubara B, Hedlund L W and Johnson G A 2005 4-D micro-CT of the mouse heart *Mol. Imaging* **4** 110–6
- Badea C T, Hedlund L W, De Lin M, Boslego Mackel J F and Johnson G A 2006 Tumor imaging in small animals with a combined micro-CT/micro-DSA system using iodinated conventional and blood pool contrast agents *Contrast Media Mol. Imaging* **1** 153–64
- Barrett H H and Myers K J 2004 *Statistical Decision Theory in Foundations of Image Science* (Hoboken, NJ: Wiley) pp 801–1000
- Boron W F and Boulpaep E L 2009 *Medical Physiology: A Cellular and Molecular Approach* (Philadelphia, PA: Saunders)
- Burvall A, Lundström U, Takman P A C, Larsson D H and Hertz H M 2011 Phase retrieval in x-ray phase-contrast imaging suitable for tomography *Opt. Express* **19** 10359–76
- Cho K and Hawkins I F 2007 *Carbon Dioxide Angiography* (London: Informa Healthcare)
- Coan P, Wagner A, Bravin A, Diemoz P C, Keyriläinen J and Mollenhauer J 2010 *In vivo* x-ray phase contrast analyzer-based imaging for longitudinal osteoarthritis studies in guinea pigs *Phys. Med. Biol.* **55** 7649–62
- Davis T J, Gao D, Gureyev T E, Stevenson A W and Wilkins S W 1995 Phase-contrast imaging of weakly absorbing materials using hard x-rays *Nature* **373** 595–8
- de Gennes P-G, Brochard-Wyart F and Quere D 2004 *Capillarity and Wetting Phenomena: Drops, Bubbles, Pearls, Waves* (New York: Springer) p 52
- Fitzgerald R 2000 Phase-sensitive x-ray imaging *Phys. Today* **53** 23–6
- Folkman J 2006 Angiogenesis *Annu. Rev. Med.* **57** 1–18
- Goodman J 2004 *Introduction to Fourier Optics* (Englewood Cliffs: Roberts and Company)
- Hanson K M 1979 Detectability in computed tomographic images *Med. Phys.* **6** 441–51
- Hemberg O, Otendal M and Hertz H M 2003 Liquid-metal-jet anode electron-impact x-ray source *Appl. Phys. Lett.* **83** 1483–5
- Hemberg O, Otendal M and Hertz H M 2004 Liquid-metal-jet anode x-ray tube *Opt. Eng.* **43** 1682–8
- Hooper S B, Kitchen M J, Siew M L, Lewis R A, Fouras A, te Pas A B, Siu K K W, Yagi N, Uesugi K and Wallace M J 2009 Imaging lung aeration and lung liquid clearance at birth using phase contrast x-ray imaging *Clin. Exp. Pharmacol. Physiol.* **36** 117–25
- Hubbell J H and Seltzer S M 2011 Tables of X-Ray Mass Attenuation Coefficients and Mass Energy-Absorption Coefficients from 1 keV to 20 MeV for Elements  $Z = 1$  to 92 and 48 Additional Substances of Dosimetric Interest <http://www.nist.gov/pml/data/xraycoef/index.cfm>

- Hwu Y, Tsai W L, Je J H, Seol S K, Kim B, Groso A, Margaritondo G, Lee K H and Seong J K 2004 Synchrotron microangiography with no contrast agent *Phys. Med. Biol.* **49** 501–8
- Kagadis G C, Loudos G, Katsanos K, Langer S G and Nikiforidis G C 2010 *In vivo* small animal imaging: current status and future prospects *Med. Phys.* **37** 6421–42
- Kiessling F *et al* 2004 Volumetric computed tomography (VCT): a new technology for noninvasive, high-resolution monitoring of tumor angiogenesis *Nat. Med.* **10** 1133–8
- Kissel L 2000 RTAB: the Rayleigh scattering database *Rad. Phys. Chem.* **59** 185–200
- Laperle C M, Hamilton T J, Wintermeyer P, Walker E J, Shi D X, Anastasio M A, Derdak Z, Wands J R, Diebold G and Rose-Petrucci C 2008 Low density contrast agents for x-ray phase contrast imaging: the use of ambient air for x-ray angiography of excised murine liver tissue *Phys. Med. Biol.* **53** 6911–23
- Laperle C M, Wintermeyer P, Wands J R, Shi D, Anastasio M A, Li X, Ahr B, Diebold G J and Rose-Petrucci C 2007 Propagation based differential phase contrast imaging and tomography of murine tissue with a laser plasma x-ray source *Appl. Phys. Lett.* **91** 173901
- Lewis R A 2004 Medical phase contrast x-ray imaging: current status and future prospects *Phys. Med. Biol.* **49** 3573–83
- Lewis R A *et al* 2005 Dynamic imaging of the lungs using x-ray phase contrast *Phys. Med. Biol.* **50** 5031–40
- Maehara N 2003 Experimental microcomputed tomography study of the 3D microangioarchitecture of tumors *Eur. Radiol.* **13** 1559–65
- Mai W, Badea C T, Wheeler C T, Hedlund L W and Johnson G A 2005 Effects of breathing and cardiac motion on spatial resolution in the microscopic imaging of rodents *Magn. Reson. Med.* **53** 858–65
- Mattson D L 2001 Comparison of arterial blood pressure in different strains of mice *Am. J. Hypertens.* **14** 405–8
- Mayo S C, Miller P R, Wilkins S W, Davis T J, Gao D, Gureyev T E, Paganin D, Parry D J, Pogany A and Stevenson A W 2002 Quantitative x-ray projection microscopy: phase-contrast and multi-spectral imaging *J. Microsc.* **207** 79–96
- Momose A 2005 Recent advances in x-ray phase imaging *Japanese J. Appl. Phys.* **44** 6355–67
- Momose A, Takeda T and Itai Y 2000 Blood vessels: depiction at phase-contrast x-ray imaging without contrast agents in the mouse and rat—feasibility study *Radiology* **217** 593–6
- Momose A, Takeda T, Itai Y and Hirano K 1996 Phase-contrast x-ray computed tomography for observing biological soft tissues *Nature Med.* **2** 473–5
- Mukundan S Jr, Ghaghada K B, Badea C T, Kao C-Y, Hedlund L W, Provenzale J M, Johnson G A, Chen E, Bellamkonda R V and Annapragada A 2006 A Liposomal nanoscale contrast agent for preclinical CT in mice *Am. J. Roentgenol.* **186** 300–7
- Paganin D, Mayo S C, Gureyev T E, Miller P R and Wilkins S W 2002 Simultaneous phase and amplitude extraction from a single defocused image of a homogeneous object *J. Microsc.* **206** 33–40
- Pfeiffer F, Weitkamp T, Bunk O and David C 2006 Phase retrieval and differential phase-contrast imaging with low-brilliance x-ray sources *Nature Phys.* **2** 258–61
- Rabin O, Manuel Perez J, Grimm J, Wojtkiewicz G and Weissleder R 2006 An x-ray computed tomography imaging agent based on long-circulating bismuth sulphide nanoparticles *Nature Mater.* **5** 118–22
- Rose A 1948 The sensitivity performance of the human eye on an absolute scale *J. Opt. Soc. Am.* **38** 196–208
- Rosina J, Kvašňák E, Šuta D, Kolářová H, Málek J and Krajčiči L 2007 Temperature dependence of blood surface tension *Physiol. Res.* **56** S93–8 (Available at [http://www.biomed.cas.cz/physiolres/pdf/56%20Suppl%201/56\\_S93.pdf](http://www.biomed.cas.cz/physiolres/pdf/56%20Suppl%201/56_S93.pdf))
- Schambach S J, Bag S, Groden C, Schilling L and Brockmann M A 2010 Vascular imaging in small rodents using micro-CT *Methods* **50** 26–35
- Svenonius O, Sahlholm A, Wiklund P and Linnros J 2009 Performance of an x-ray imaging detector based on a structured scintillator *Nucl. Instrum. Methods A* **607** 138–40
- Tuohimaa T, Otendal M and Hertz H M 2007 Phase-contrast x-ray imaging with a liquid-metal-jet-anode microfocus source *Appl. Phys. Lett.* **91** 074104
- Vlassenbroeck J, Dierick M, Masschaele B, Cnudde V, Van Hoorebeke L and Jacobs P 2007 Software tools for quantification of x-ray microtomography at the UGCT *Nucl. Instrum. Methods A* **580** 442–5
- Wilkins S W, Gureyev T E, Gao D, Pogany A and Stevenson A W 1996 Phase-contrast imaging using polychromatic hard x-rays *Nature* **384** 335–8
- Zhang X, Liu X-S, Yang X-R, Chen S-L, Zhu P-P and Yuan Q-X 2008 Mouse blood vessel imaging by in-line x-ray phase-contrast imaging *Phys. Med. Biol.* **53** 5735